

Angstrom-Size Defect Creation and Ionic Transport through Pores in Single-Layer MoS₂

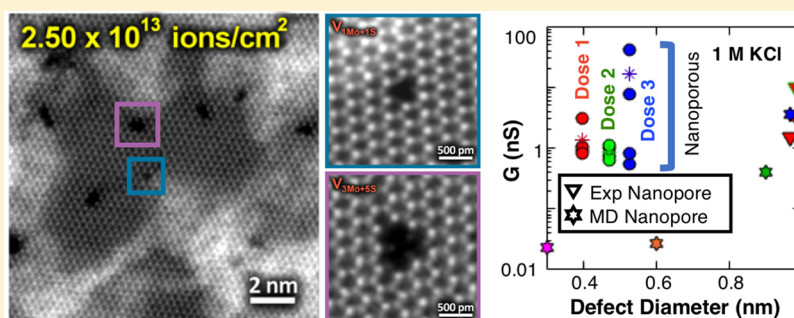
Jothi Priyanka Thiruraman,^{†,‡,§} Kazunori Fujisawa,[§] Gopinath Danda,^{†,‡,§} Paul Masih Das,^{†,§} Tianyi Zhang,[⊥] Adam Bolotsky,[§] Néstor Perea-López,[§] Adrien Nicolai,[#] Patrick Senet,[#] Mauricio Terrones,^{§,||,⊥} and Marija Drndić^{*,†,§}

[†]Department of Physics and Astronomy and [‡]Department of Electrical and Systems Engineering, University of Pennsylvania, Philadelphia, Pennsylvania 19104, United States

[§]Department of Physics, Center for 2-Dimensional and Layered Materials, ^{||}Department of Chemistry, and [⊥]Department of Materials Science and Engineering, The Pennsylvania State University, University Park, Pennsylvania 16802, United States

[#]Laboratoire Interdisciplinaire Carnot de Bourgogne UMR 6303 CNRS-Université de Bourgogne Franche Comté, 9 Avenue Alain Savary, BP 47870, F-21078 Dijon Cedex, France

S Supporting Information



ABSTRACT: Atomic-defect engineering in thin membranes provides opportunities for ionic and molecular filtration and analysis. While molecular-dynamics (MD) calculations have been used to model conductance through atomic vacancies, corresponding experiments are lacking. We create sub-nanometer vacancies in suspended single-layer molybdenum disulfide (MoS₂) via Ga⁺ ion irradiation, producing membranes containing ~300 to 1200 pores with average and maximum diameters of ~0.5 and ~1 nm, respectively. Vacancies exhibit missing Mo and S atoms, as shown by aberration-corrected scanning transmission electron microscopy (AC-STEM). The longitudinal acoustic band and defect-related photoluminescence were observed in Raman and photoluminescence spectroscopy, respectively. As the irradiation dose is increased, the median vacancy area remains roughly constant, while the number of vacancies (pores) increases. Ionic current versus voltage is nonlinear and conductance is comparable to that of ~1 nm diameter single MoS₂ pores, proving that the smaller pores in the distribution display negligible conductance. Consistently, MD simulations show that pores with diameters <0.6 nm are almost impermeable to ionic flow. Atomic pore structure and geometry, studied by AC-STEM, are critical in the sub-nanometer regime in which the pores are not circular and the diameter is not well-defined. This study lays the foundation for future experiments to probe transport in large distributions of angstrom-size pores.

KEYWORDS: Nanopores, MoS₂, ion-beam damage, desalination, ion transport

Ionic and molecular transport through individual solid-state nanopores has been studied thanks to the ability to fabricate nanometer scale holes in thin membranes.¹ In contrast, ionic transport through smaller, sub-nanometer pores and nanoporous two-dimensional (2D) membranes has not yet been explored in detail, although these systems present fascinating opportunities to study phenomena at the atomic scale. Most studies infer the conductance and sub-nanometer pore diameters indirectly from modeling.^{2,3} With the recent availability of 2D materials⁴ that can be suspended as membranes⁵ and the ability to image atomic-scale defects,⁶ it is now possible to study the fundamental principles behind ion

flow through sub-nanometer pores.³ A few recent papers have reported transport measurements in individual molybdenum disulfide (MoS₂) sub-nanometer pores.^{7,8}

Thin nanoporous membranes containing a large number of pores provide opportunities for fluid filtration, molecular analysis, and energy generation. In water-desalination applications, there is a demand for high-throughput, where atomic-scale pores (atomic vacancies in the material) provide unique

Received: October 24, 2017

Revised: January 31, 2018

Published: February 21, 2018

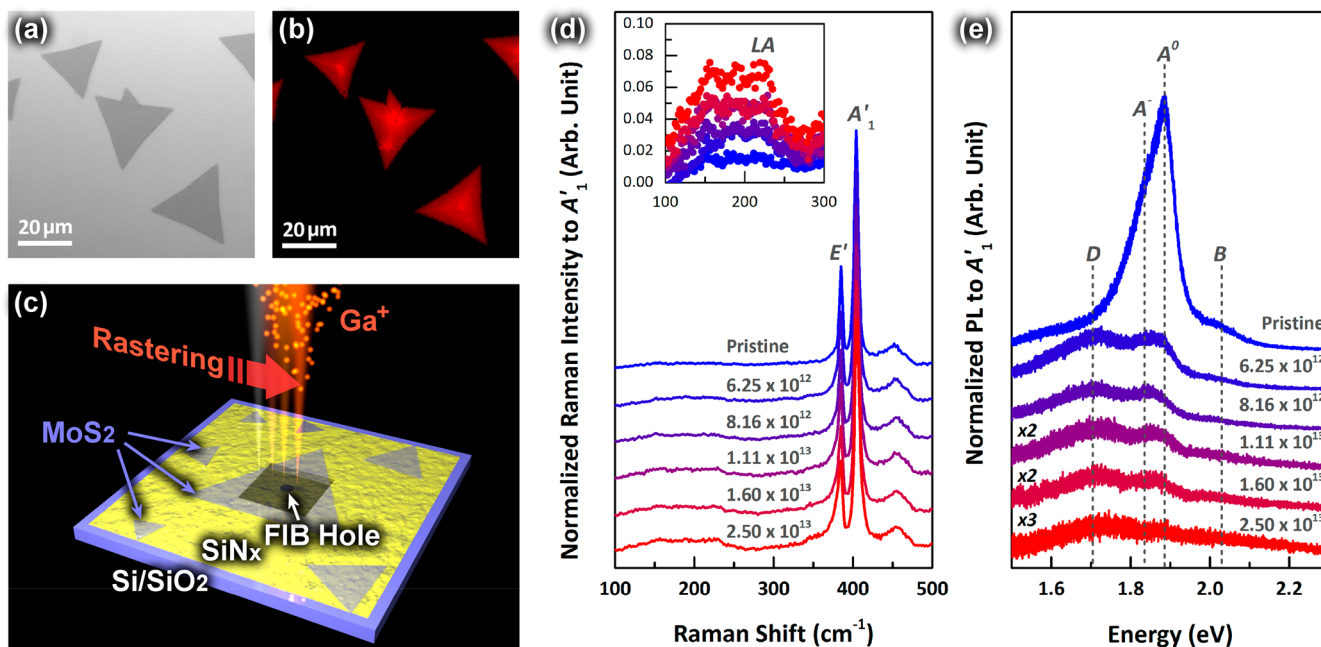


Figure 1. (a) Optical image and (b) fluorescence image (673 nm centered bandpass filtered) of as-grown single-layer MoS₂. (c) Schematic illustration of focused Ga⁺ ion beam based irradiation process. (d) Raman and (e) photoluminescence spectra of the pristine and the Ga⁺ ion irradiated MoS₂.

benefits. This is because (i) water transport scales inversely with membrane thickness allowing for high water fluxes and (ii) membranes with sub-nanometer pores are highly selective.^{9–12} Previous experiments explored ionic transport in nanoporous graphene membranes.^{10,13,14} Heirianian et al. indicated the benefits of MoS₂ pores compared to graphene.¹⁵ To the best of our knowledge, there have been no studies of transport in nanoporous MoS₂ membranes.

Here, we report ionic transport measurements through MoS₂ membranes with a population of sub-nanometer pores introduced by controlled Ga⁺ ion irradiation at 30 kV. We study the vacancy defects and the resulting properties of the suspended MoS₂ lattices using AC-STEM, Raman spectroscopy, and photoluminescence (PL) spectroscopy. We observe the longitudinal acoustic (LA) band and defect-related PL and determine the vacancy-defect size distribution as a function of Ga⁺ ion irradiation dose, showing the median defect diameter in the range of 0.3–0.4 nm.

Single-layer MoS₂ triangular-flakes were synthesized via a halide-assisted powder vaporization method (Figure 1a).¹⁶ The presence of single-layer material was confirmed by fluorescence microscopy (Figure 1b, 673 nm bandpass filtered). While single-layer MoS₂ shows strong photoluminescence, the signal is quenched in multilayered MoS₂.¹⁷ Similar to graphene,¹⁸ polycrystalline MoS₂ fractures at grain boundaries under strain.¹⁹ To maintain the rigidity of the material, we focused on single crystal MoS₂. Single-layer MoS₂ flakes were transferred onto carbon grids²⁰ or SiN_x⁵ using a polymethyl methacrylate-assisted transfer (Figures S1 and S2). Atomic vacancy-defects were introduced by rastering the Ga⁺ ion probe over a certain area (Figure 1c) using a focused ion beam (FIB).^{21,22} The degree of defectiveness was controlled by varying the Ga⁺ ion dose from 6.25 × 10¹² ions/cm² (see Figure S3) until the PL signal of the irradiated MoS₂ fell into noise level (2.50 × 10¹³ ions/cm²). After prolonged irradiation, the fluorescence signal was suppressed regardless of dose.

The effect of Ga⁺ ion irradiation on MoS₂ flakes was investigated by Raman spectroscopy and PL spectroscopy (panels d and e of Figure 1, respectively). After Ga⁺ ion irradiation of the MoS₂, several Raman peaks located around 200 cm⁻¹, in the vicinity of the longitudinal acoustic (LA) band emerged, whereas the first-order in-plane (E') and out-of-plane (A₁') modes remained unaffected.²¹ The LA band consists of several peaks including LA (~M), LA (~K), and a van Hove singularity at the saddle point between the K- and M-points in the Brillouin zone.²² Because these LA (~M) and LA (~K) modes far from the Γ-point are only activated when defects are introduced into the MoS₂ lattice, their relative intensity with respect to the A₁' mode ($I(\text{LA})/I(\text{A}'_1)$) can be used as an indicator of the degree of crystallinity.^{21,22} The relative intensity, $I(\text{LA})/I(\text{A}'_1)$ increased with higher Ga⁺ ion doses (see the inset of Figure 1d), as expected.

The PL of the MoS₂ flakes was found to be sensitive to ion irradiation.²³ For pristine MoS₂, there were two peaks at 1.88 and 2.03 eV in the PL spectra, corresponding to the A and B exciton peaks. The A exciton peak was composed of two subpeaks with energy at 1.88 eV (neutral exciton: A⁰) and 1.82 eV (trion: A⁻).²⁴ After Ga⁺ ion irradiation, the neutral exciton A⁰ was suppressed and a new peak, a bound exciton (D) located at ~1.72 eV, emerged. This newly emerged photoemission peak can be correlated to defect-mediated radiative recombination processes.^{23,25,26} The bound exciton peak is also observed when the MoS₂ is irradiated by α-particles²³ and energetic plasma.²⁵ The spectral weight of the bound exciton peak becomes higher with increasing Ga⁺ ion dose, similar to the relative intensity of the LA band, and at a dose of 2.5 × 10¹³ ions/cm², the PL intensity becomes close to the noise level. The enhancement of the LA band and the suppression of the neutral exciton reflect a qualitative increase of defectiveness (e.g., number and size of vacancies), within MoS₂ monocrystals after the Ga⁺ ion irradiation. However, upon the collision between an ion and an atom, several different types of defects

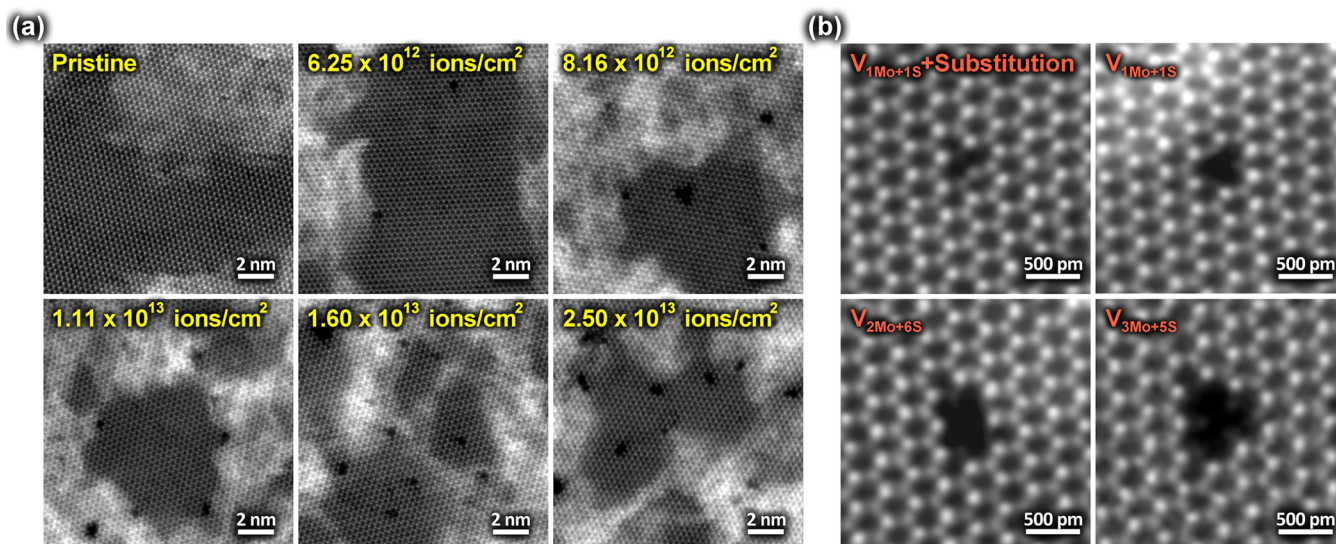


Figure 2. Aberration corrected scanning transmission electron microscopy (AC-STEM) characterization of single-layer MoS₂. (a) AC-STEM image of the pristine and the Ga⁺ ion irradiated MoS₂ with different ion doses. (b) High-magnification AC-STEM image of atomic vacancies with different atomic configuration. These images were used to perform the statistical analysis of defects shown in Figure S7 and are described in the text.

including topological defects, atomic vacancies, holes, and amorphous regions can form⁴ depending on the ion species and their kinetic energy.²⁷ A quantitative study of vacancy-defects; such as type, density and edge termination of defects, is required but cannot be completed using only the techniques above. In this context, Surwade et al. mentioned that even when similar optical signatures were observed in differently prepared defective graphene membrane, the water-transport properties of the membranes varied.⁹

In 2D systems, the type of vacancy-defects introduced by ion irradiation changes depending on the ion characteristics and kinetic energy.^{28,29} For the electron irradiation of MoS₂ using a parallel beam, monosulfur vacancies (V_S) and disulfur vacancies (V_{2S}) are predominant.^{6,27} With increased electron irradiation time, sulfur vacancies migrate and aggregate into line defects.³⁰ In contrast to electrons, the mass of an ion is larger and varies, resulting in ion-species-dependent effects. Molecular dynamics (MD) simulations suggest that higher mass causes more displacement and sputtering of atoms.^{28,29} Direct observation of vacancy-defects created by Ga⁺ ion irradiation is needed to fully understand their characteristics.

Ion-irradiated MoS₂ membranes were investigated by aberration-corrected scanning transmission electron microscopy (AC-STEM). Figure 2a shows high-angle annular dark-field (HAADF) images of MoS₂ before and after Ga⁺ ion irradiation for different doses: 0 (pristine), 6.25×10^{12} , 8.16×10^{12} , 1.11×10^{13} , 1.60×10^{13} , and 2.50×10^{13} ions/cm². HAADF intensity changes depending on $\sim Z^2$ (Z : atomic number), allowing us to roughly distinguish elements (Mo or S) and, therefore, the atomic configuration of vacancy-defects. Figure 2b shows magnified STEM-HAADF images of several atomic vacancies. Metal atomic vacancies with several sulfur vacancies ($V_{x\text{Mo}+y\text{S}}$) are formed rather than sulfur vacancies (V_S), topological defects (bond changing), or amorphous regions. This is consistent with expected sputtering behavior due to the relatively higher mass of Ga⁺ in comparison to electrons and leads to disulfur or monosulfur termination-rich edge structures.

To investigate the effect of the Ga⁺ ion dose on pore (i.e., vacancy-defect) area and density, statistical analysis was performed on AC-STEM images (see Figure S7). Within the

irradiation dose ranges we used, the pore density increases with larger doses, whereas the pore area remains roughly constant. For the lowest dose (6.25×10^{12} ions/cm²), the majority of the atomic pores were single-molybdenum-based vacancies ($V_{1\text{Mo}+y\text{S}}$), while the number of missing sulfur atoms varied. With increasing Ga⁺ ion dose, the number of double-molybdenum-based vacancies ($V_{2\text{Mo}+y\text{S}}$) increased, and some triple-molybdenum-based vacancies were also found ($V_{3\text{Mo}+y\text{S}}$; Figure 2b), exhibiting low-intensity STEM-HAADF signals inside the defect. Because these defects were observed far from carbon contamination caused by the transfer process (Figure S4) and the STEM-HAADF intensity was close to V_S , we assigned the structure inside the defect to sulfur. When the Ga⁺ ion dose reached 2.50×10^{13} ion/cm², the density of pores with size >0.8 nm in diameter increased (see Figure S7).

To observe the ionic transport characteristics of the angstrom-size defects in the MoS₂ membranes, we implement the device setup shown in Figure 3a. A MoS₂ flake was selected under an optical microscope and then transferred over a SiN_x window with a ~ 200 nm diameter FIB hole (Figure S1).^{31,32} The membrane was then irradiated with doses ranging from 6.25×10^{12} to 2.50×10^{13} ions/cm² to create atomic vacancies with average single defect diameters between 0.4 and 0.5 nm. The top inset of Figure 3b shows a STEM image of a suspended MoS₂ membrane over a FIB hole exposed with a dose of 2.50×10^{13} ions/cm². A resultant nonlinear current-voltage (I - V) curve is shown in Figure 3b for an irradiated MoS₂ membrane (device P, dose of 1.60×10^{13} ions/cm²). For comparison, a similar trace is shown in the bottom inset for a pristine sample demonstrating a baseline ionic conductance ($G = dI/dV$) of ~ 10 pS.

Figure 3c,d show ionic current traces at $V_B = 0.1$ V and the corresponding current noise for two devices (dose of 1.60×10^{13} ions/cm²). It should be noted that only those devices are shown here that have an ionic conductance of $G > 5$ nS in the range of ± 0.1 V. For devices exhibiting $G < 5$ nS, the defects are too small to allow significant ionic flow below a certain threshold voltage (discussed below), thus making ionic noise extraction difficult. The power spectral density was extracted from the current traces and fit to the following equation:

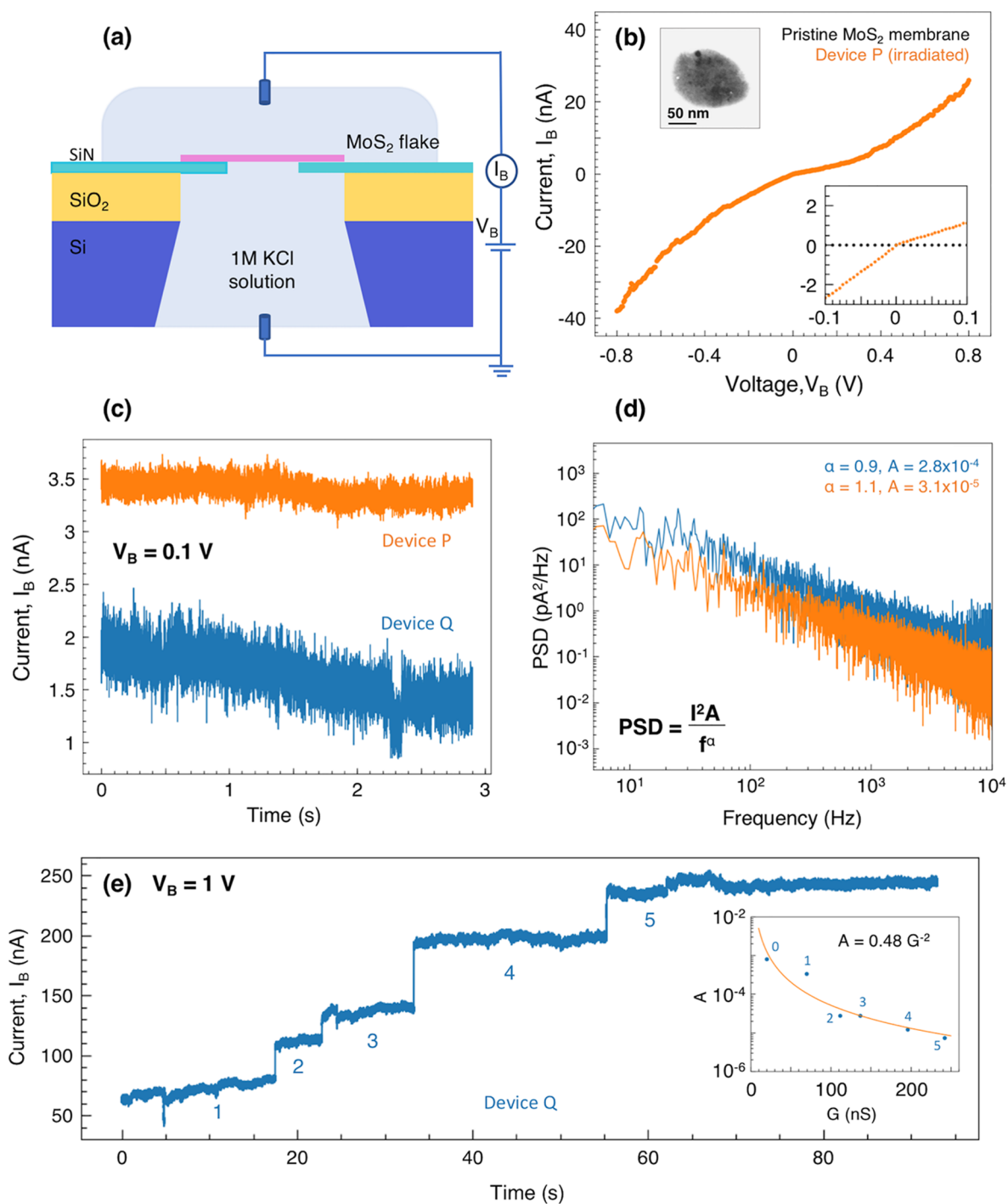


Figure 3. (a) Experimental setup to measure the conductance of nanoporous MoS₂ membranes. (b) Current–voltage plot of a MoS₂ device irradiated with a dose of 1.60×10^{13} ions/cm² showing a nonlinear trend in the voltage range of $V_B = \pm 0.8$ V (orange, device P). (bottom inset) Current–voltage curves for a pristine MoS₂ membrane (black) and the same irradiated MoS₂ device for $V_B = \pm 0.1$ V. (top inset) STEM image of a suspended MoS₂ membrane exposed to a Ga⁺ ion dose of 2.50×10^{13} ions/cm². (c) Current vs time traces at an applied voltage of $V_B = 0.1$ V and (d) the corresponding power spectral density for two devices (device P and Q, dose of 1.60×10^{13} ions/cm²). (e) Current vs time trace for device Q at an applied voltage of $V_B = 1$ V showing an increase in conductance in steps, suggesting membrane damage. (inset) Noise at an initial conductance of 20 nS before the high-voltage induced damage (zeroth point) is obtained from panel d.

$$\text{PSD} = \frac{I^2 A}{f^\alpha} \quad (1)$$

where PSD is the power spectral density, I is the corresponding ionic current, f is the frequency, A is the noise coefficient, and α is the low-frequency noise exponent. All of the devices showed a noise exponent value of $\alpha \approx 1$ and noise coefficient of $A \approx$

10^{-4} – 10^{-5} , suggesting dominant low-frequency noise as has been demonstrated previously in 2D nanopore devices.^{31,33,34}

To further investigate the stability of our devices, we applied a constant $V_B = 1$ V and monitored the change in ionic current for another device with the same dose (device Q, dose = 1.60×10^{13} ions/cm²), as shown in Figure 3e. The current increased in jumps from 20 nA (from Figure 3c) to 250 nA, suggesting

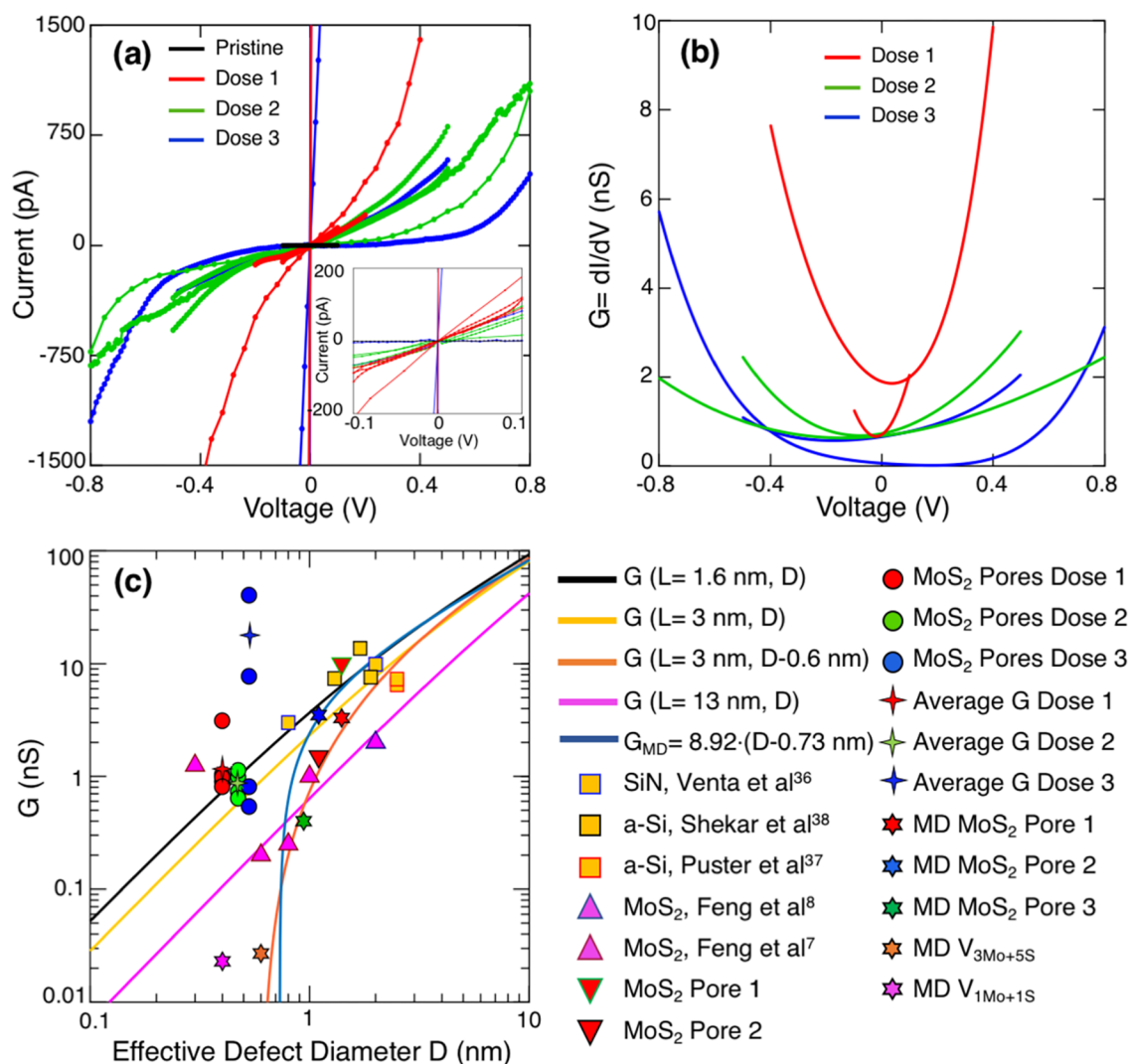


Figure 4. (a) Ionic current vs voltage (I – V) curves measured for pristine and irradiated MoS₂ membranes with dose 1 (6.25×10^{12} ions/cm²), dose 2 (1.11×10^{13} ions/cm²), and dose 3 (2.5×10^{13} ions/cm²). The applied sweep rate was between 5 and 20 mV per second. (b) Corresponding dI/dV with respect to voltage for nonlinear I – V curves in panel a. (c) Conductance G is shown as a function of the pore diameter for both the continuum (black, yellow, orange, and pink) and molecular dynamics (MD) simulated (blue) models. Plotted are also G values from the MD model discussed in the text for five pores shown in Figure S5, the experimentally obtained G values for MoS₂ nanoporous membranes and single nanopores, and reported values from previous works on SiN,³⁶ a-Si,^{37,38} and MoS₂ nanopores.^{7,8}

incremental damage of the membrane as opposed to gradual increase of defect sizes.³⁵ The noise coefficients extracted from each section and plotted in the inset (zeroth point is from Figure 3c) reveal that the low-frequency noise decreases with increasing conductance, in accordance with a power law:

$$A = 0.48G^{-2} \quad (2)$$

A similar trend of increasing conductance was also observed in other devices when V_B exceeded ± 0.8 V. To ensure that we did not damage our devices during ionic experiments, V_B was kept in the range of ± 0.5 V for most of our devices.

Figure 4a presents the I – V curves for a pristine membrane and 15 devices irradiated at three different doses (dose 1 = 6.25×10^{12} , dose 2 = 1.11×10^{13} , and dose 3 = 2.50×10^{13} ions/cm²). We note that while a total of 25 devices were irradiated and tested, 10 of these yielded negligible ionic conductance ($G \approx 10$ pS) comparable to non-irradiated, i.e., pristine samples, close to our detection limit, and are not shown here. In Figure 4a, several of the 15 I – V curves plotted overlap (6 red, dose 1;

4 green, dose 2; 5 blue, dose 3; 1 black, pristine). A total of six representative differential conductances (dI/dV) for doses 1–3 are shown in Figure 4b. Collective current passing through multiple angstrom-size pores in a MoS₂ membrane resulting in nonlinear I – V curves at voltages $V_B \geq 0.1$ V are displayed by $\sim 80\%$ of the devices. At lower voltages ($V_B < 0.1$ V), the I – V curves are linear (Figure 4a inset). Such nonlinear trends have been observed previously for sub-nanometer 2D pores and were attributed to stripping of the ionic solvation shell at higher driving voltages.^{3,7} About 20% of devices showed higher conductance ($G > 5$ nS) and a linear trend, even up to 1 V. This may be due to the merging of individual angstrom-size pores or their enlargement over time, resulting in higher conductance values and linear I – V curve behavior that is typically observed in nanometer-size pores that are well-described by the continuum model.⁷

Using the previously stated AC-STEM analysis (Figure S7), we estimate the number of pores, N , and their diameters, D , within the nanoporous membranes for the various doses. The

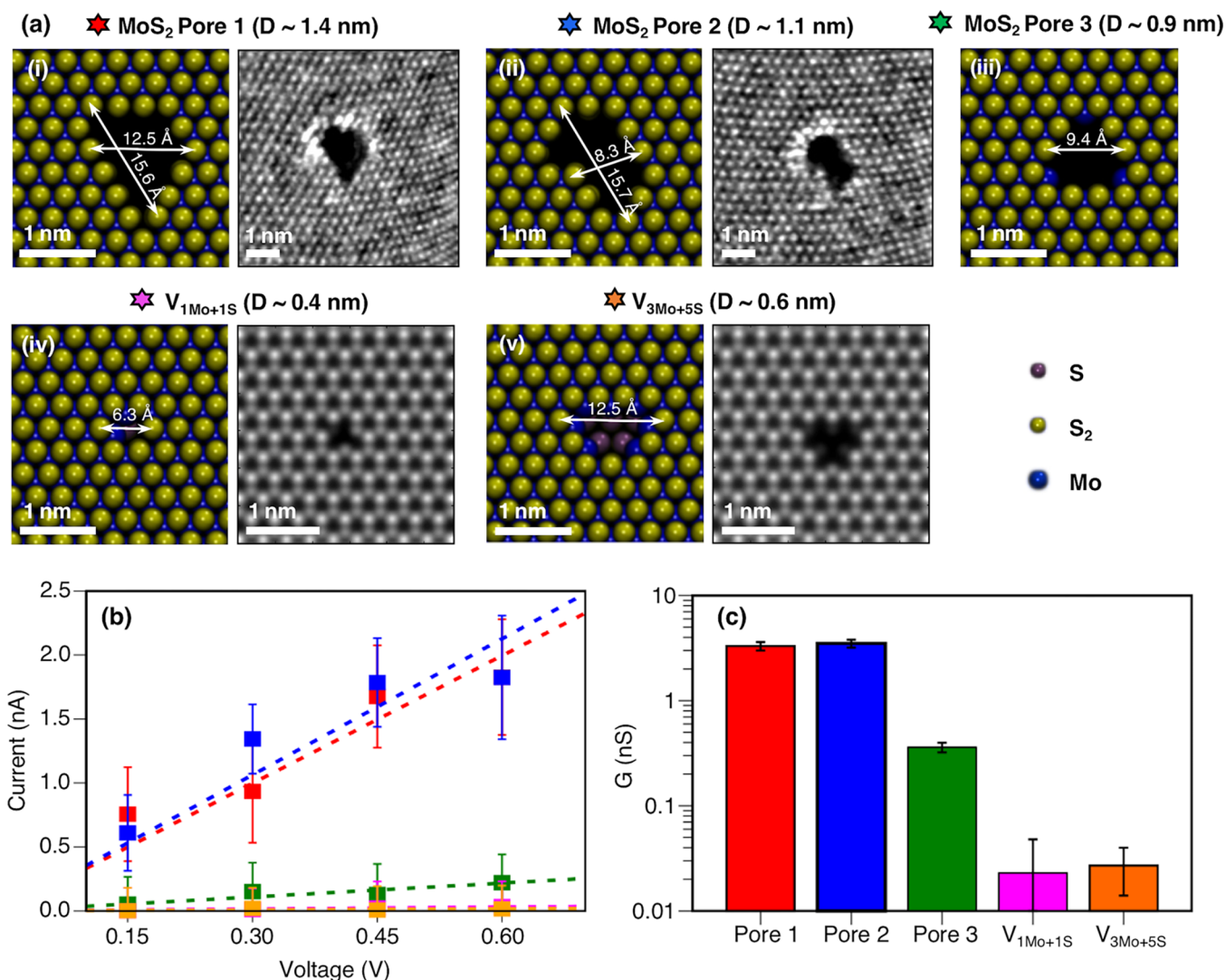


Figure 5. (a) AC-STEM images of individual MoS₂ pores: (i) pore 1 and (ii) pore 2 with effective diameters of ~1.4 and 1.1 nm, respectively. Corresponding all-atom structures used in non-equilibrium molecular dynamics (NEMD; see section 10 of the Supporting Information) simulations are presented aside. Mo, S₂, and S atoms are shown in blue, yellow, and purple spheres, respectively. (iii) Atomic structure of an equivalent circular pore of diameter of ~0.9 nm. QSTEM simulations⁴¹ for vacancy-defects caused by (iv) 1Mo and 1S (V_{1Mo+1S}) missing and (v) 3Mo and 5S atoms (V_{3Mo+5S}). (b) *I*–*V* characteristics and (c) conductance *G* panel computed from NEMD simulations for the five pores shown in panel a. Error bars represent the standard deviation from the ionic current computed from NEMD runs.

mean and maximum diameters of pores are 0.4 and 0.8 nm for dose 1, 0.5 and 0.9 nm for dose 2, and 0.5 and 1.3 nm for dose 3, respectively. The number of pores ranges from $N \approx 300$ for dose 1, $N \approx 700$ for dose 2, and $N \approx 1200$ for dose 3. This is estimated using the results from Figure S7a and calculating how many pores of average diameter are contained in the suspended area $\sim 3 \times 10^4 \text{ nm}^2$. From the defect size distributions, we also estimate the number of pores with diameters larger than the hydrated K⁺ ion diameter (the smaller ion compared to Cl⁻),³⁹ where $D > 0.6 \text{ nm}$: ~30, ~120 and ~240 for doses 1–3, respectively. Similarly, the estimated number of pores with $D \geq 1 \text{ nm}$ are zero for doses 1 and 2 and ~34 for dose 3. Doses 1–3 were chosen because they produce well-separated, angstrom-size defects. For higher doses, defects start to merge resulting in larger, irregularly shaped pores.

Despite a large number of defects, most of them are very small, below $\sim 5 \text{ \AA}$. Based on molecular dynamics simulations,¹⁵ such pores are expected to be too small for ions to flow through but should allow water molecules to pass. We therefore expect

the measured conductance in the range of $V_B = \pm 0.1 \text{ V}$ of the irradiated MoS₂ membranes to be low, and indeed, it was found to be $\sim 1 \text{ nS}$ in 80% of the devices shown in Figure 4a. The average conductances of the irradiated devices were $\sim 1 \text{ nS}$ for doses 1 and 2, increasing to $\sim 10 \text{ nS}$ for dose 3. We compare and contrast the irradiated membranes to single nanopore devices in Figure 4c, which plots the conductances of the nanoporous membranes as a function of the effective defect diameter (including the mean *G* for each dose), as well as the conductances of two single MoS₂ nanopore devices that were drilled using AC-STEM with effective *D* values of ~1.4 and ~1.1 nm (shown in Figure 5a(i),(ii)). Effective *D* is defined as *D* of a circle with the same area as the pore (calculated using ImageJ software). We also compare our results with previously published literature on single pores (less than 2 nm in diameter) in MoS₂,^{7,8,40} thinned silicon nitride,³⁶ and amorphous silicon membranes with $D \approx 0.3$ to 2 nm.^{37,38}

The average conductance measured for dose 1 is $\sim 1.4 \text{ nS}$, slightly higher than that of dose 2 ($1.11 \times 10^{13} \text{ ions/cm}^2$),

where the measured average conductance is 0.9 nS. While the larger dose 2 is expected to give larger mean conductance than dose 1, the averaged experimental results can be explained by the following two factors: (i) the mean vacancy sizes obtained from these two doses are very close to each other, i.e., 0.4 and 0.5 nm for dose 1 and dose 2, respectively, as shown in Figure S7; and (ii) the spread in the conductance values for different samples, irradiated at each dose, is larger than the difference between the averages of the two doses. Dose 3 (2.5×10^{13} ions/cm²), which is the highest dose used, yielded the largest mean conductance (~ 10 nS), consistent with expectations that samples irradiated with larger doses yield higher ionic conductance.

We observe variation of 2 orders of magnitude in the experimental conductance values corresponding to single pores and nanoporous membranes, from $G \approx 0.1$ to 10 nS for single pores with $D \approx 0.3$ to 2 nm, and $G \approx 1$ to 100 nS for nanoporous devices with an average D of ≈ 0.5 nm. This enhancement in conductance is expected due to the presence of multiple nanopores. However, the scatter among devices could come from several reasons, including the variations in atomic structure and edge terminations that can result in different properties of the pores when they are introduced in the salt solutions. This has not yet been explored experimentally. It is also challenging to determine the diameter accurately. The effective D used on the x -axis is measured from AC-TEM images with pores in vacuum before ionic measurements, and it can change later (for example, due to expansion or contamination in solution).³²

To estimate the conductance of the pores with precise and stable diameters, we perform molecular dynamics simulations⁴² (see sections 9 and 10 in the Supporting Information). Figure Sai–v shows the five configurations that were tested, where pores 1 and 2 (the same as in Figure 5c) correspond to AC-STEM drilled MoS₂ pores with effective diameters of ~ 1.4 and 1.1 nm, respectively (see Figure S9), and pore 3 corresponds to a perfectly circular pore of effective diameter 0.9 nm, and finally, $V_{1\text{Mo}+1\text{S}}$ and $V_{3\text{Mo}+5\text{S}}$, which represent the defect vacancies with one of the smallest and largest diameters, respectively (Figure S7). The conductances of these five pores are plotted in Figure 4c. As shown in Figure 5b, I – V curves were computed for each system via MD simulations, and conductances G were obtained by the linear fitting of I – V curves with $0.15 \text{ V} < V_{\text{B}} < 0.6 \text{ V}$. Figure 5c presents the conductance obtained for all the simulated pores, showing a variation of 3 orders of magnitude depending on the pore size. Pores 1 and 2 are characterized by conductance values of 3.3 and 3.5 nS, respectively, which agree within a factor of 2–3 with the experimental values (~ 10 and 1.5 nS in Figure 4c), while pore 3 shows a conductance of 0.4 nS. The conductance G drops drastically for pore 3 because of its smaller diameter in comparison with pore 1 and 2 and because its diameter is close to the limiting diameter value for zero conductance. Finally, pores made of defects $V_{1\text{Mo}+1\text{S}}$ ($D \approx 0.4$ nm) and $V_{3\text{Mo}+5\text{S}}$ ($D \approx 0.6$ nm) exhibited a negligible conductance of $G \approx 0.02$ – 0.03 nS, confirming the fact that pores made of defects smaller than ~ 0.6 nm do not conduct ions in our experiments.

In this size range (< 1 nm), small changes in D by ~ 0.1 nm result in conductance changes by 1 order of magnitude or more (notice the sharp drop of the blue line in Figure 4c). Using the MD simulations, we obtain an empirical linear model of open conductance for MoS₂ pores less than 3 nm, plotted as the blue line in Figure 4c:

$$G_{\text{MD}} = C(D - D_{\text{min}}) \quad (3)$$

where G_{MD} is the pore conductance derived from MD, $C = 8.92$ S/m is the conductivity of KCl ions through single-layer MoS₂ nanopores less than 3 nm, and $D_{\text{min}} = 0.73$ nm is the minimum pore diameter for ionic flow. Furthermore, in Figure 4c, this model derived from MD simulations⁴² is featured as a blue line along with the black, yellow, pink, and orange fit lines $G(L$ and $D)$, which represent the continuum model for the conductance for different values of pore thickness, L .

Ionic measurements have validated the continuum model for pores with nanometer-scale diameters and shown that an effective pore thickness, $L \approx 1.6$ nm is a good approximation for MoS₂.⁴³ This corresponds to the black line in Figure 4c. Here, the pore is modeled as a system of three resistors in series. The interior of the nanopore is modeled as a cylindrical resistor, $R_{\text{p}} = \frac{1}{\sigma} \frac{4L}{\pi D^2}$, where σ is the conductivity of the electrolyte, L is the thickness of the nanopore, and D is its diameter. Additionally, there is an access resistance in series on each side where current paths converge from the bulk electrolyte into the pore,⁴⁴ $R_{\text{a}} = \frac{1}{\sigma} \frac{1}{2D}$. The total resistance of the single nanopore, R_{t} , is given by the sum of the three resistances, the interior of the nanopore and two access resistances:

$$R_{\text{t}} = R_{\text{p}} + 2R_{\text{a}} = \frac{1}{\sigma} \left(\frac{4L}{\pi D^2} + \frac{1}{D} \right) \quad (4)$$

This gives us an equation for conductance through a single nanopore of diameter D and thickness L :

$$G_{\text{t}} = \frac{\sigma \pi D^2}{4L + \pi D} \quad (5)$$

We stress that $G(L = 1.6 \text{ nm}, D)$ does not fit the conductance measured in single MoS₂ sub-nanometer pores plotted in Figure 4c, in contrast to the agreement found in pores with larger diameters ($D > 1$ nm). In fact, the data clearly show that small pores conduct less than expected from this model, and a better fit can be obtained by assuming a larger pore thickness (the pink line in Figure 4c where $L = 13$ nm) or by assuming an effectively smaller diameter. The orange line, $G(L = 1.6 \text{ nm}, D - 0.6 \text{ nm})$ corresponds to a continuum model, assuming that the pore diameter is smaller than the actual diameter by 0.6 nm, meaning that a pore with $D = 0.6$ nm would give zero current. This best fit is also consistent with the assumption that for a KCl ionic solution, K⁺ is the smallest hydrated ion with a diameter of 0.6 nm, such that a pore diameter, $D = 0.6$ nm, will effectively resist the transport of ions.^{3,39} This model closely resembles the linear model of conductance obtained from MD simulations for pores smaller than 2 nm. For large D , $G(L = 1.6 \text{ nm}, D = 0.6 \text{ nm}) \approx G(L = 1.6 \text{ nm}, D)$, and the two models converge (orange and black lines). To our knowledge, besides these data points, the only comparable pores that have been measured in the diameter range of less than 2 nm are Si/SiO₂ pores³⁶ and ultrathin Si₃N₄.^{34,35} The corresponding fit $G(L = 3 \text{ nm}, D)$ is shown in yellow for comparison to $G \approx 3$ to 10 nS for $D \approx 0.8$ to 2 nm.

In conclusion, we created nanoporous MoS₂ membranes containing ~ 100 – 1000 angstrom-size pores with a mean diameter of ~ 0.5 nm, and the devices were characterized by atomic-resolution imaging and Raman and PL spectroscopy. The measured conductance in 80% of the devices was of the

order of 1 nS. We have also fabricated two single ~ 1 nm diameter MoS_2 pores with corresponding AC-STEM images, and G was found to be ~ 1 and 10 nS. Our experiments and comparison with single-pore data demonstrate that conductance must occur only through the few larger pores within the distribution and that the majority of the defects do not allow ions to pass through. These results have a direct application for water desalination. Our MD simulations reveal that the defects with diameters less than ~ 0.6 nm are too small for ions to go through and result in negligible conductance < 20 pS. This conductance is comparable to the conductance obtained in a controlled experiment using a pristine membrane. Future studies may use atomic-resolution imaging to correlate the ionic transport measurements with the detailed information on the atomic structure of the individual conducting defects. Furthermore, there is a need for the modeling of nanoporous membranes containing a large distribution of angstrom-size pores that can now be fulfilled using the AC-STEM insights provided by this work.

■ ASSOCIATED CONTENT

Supporting Information

The Supporting Information is available free of charge on the ACS Publications website at DOI: [10.1021/acs.nanolett.7b04526](https://doi.org/10.1021/acs.nanolett.7b04526).

Additional information on the fabrication of devices, the transfer of single-layer MoS_2 , the control of defects, Raman and photoluminescence spectroscopy, AC-STEM analysis, simulation of HAADF images, ionic measurements, calculation of effective diameters of noncircular pores, and non-equilibrium molecular dynamics. (PDF)

■ AUTHOR INFORMATION

Corresponding Author

*E-mail: drndic@physics.upenn.edu.

ORCID

Jothi Priyanka Thiruraman: 0000-0001-5089-491X

Gopinath Danda: 0000-0003-3455-3474

Paul Masih Das: 0000-0003-2644-2280

Tianyi Zhang: 0000-0002-8998-3837

Patrick Senet: 0000-0002-2339-0019

Marija Drndić: 0000-0002-8104-2231

Author Contributions

J.P.T. and K.F. contributed equally. The manuscript was written through contributions of all authors. All authors have given approval to the final version of the manuscript.

Notes

The authors declare no competing financial interest.

■ ACKNOWLEDGMENTS

This work was funded by NIH grant nos. R21HG007856 and R01HG006879 and NSF grant no. EFRI 2-DARE (EFRI-1542707). We thank William Parkin and Francis Chen-Chi Chien for their generous help in fabricating and measuring the single MoS_2 pores used in Figures 4 and 5. We greatly acknowledge the use of JEOL JEM ARM200CF at Lehigh University. MoS_2 single pores were drilled with the help of the facility. The calculations were performed using HPC resources from DSI-CCuB (Université de Bourgogne). The theoretical work was supported by a grant from the Air Force Office of Scientific Research (AFOSR) as part of a joint program with

the Directorate for Engineering of the National Science Foundation (NSF), Emerging Frontiers and Multidisciplinary Office grant no. FA9550-17-1-0047.

■ REFERENCES

- (1) Branton, D.; Deamer, D. W.; Marziali, A.; Bayley, H.; Benner, S. A.; Butler, T.; Di Ventra, M.; Garaj, S.; Hibbs, A.; Huang, X.; Jovanovich, S. B.; Krstic, P. S.; Lindsay, S.; Ling, X. S.; Mastrangelo, C. H.; Meller, A.; Oliver, J. S.; Pershin, Y. V.; Ramsey, J. M.; Riehn, R.; Soni, G. V.; Tabard-Cossa, V.; Wanunu, M.; Wiggin, M.; Schloss, J. A. *Nat. Biotechnol.* **2008**, *26* (10), 1146–1153.
- (2) Rollings, R. C.; Kuan, A. T.; Golovchenko, J. A. *Nat. Commun.* **2016**, *7*, 11408.
- (3) Jain, T.; Rasera, B. C.; Guerrero, R. J. S.; Boutilier, M. S. H.; O'Hern, S. C.; Idrobo, J.-C.; Karnik, R. *Nat. Nanotechnol.* **2015**, *10* (12), 1053–1057.
- (4) Lin, Z.; Carvalho, B. R.; Kahn, E.; Lv, R.; Rao, R.; Terrones, H.; Pimenta, M. A.; Terrones, M. *2D Mater.* **2016**, *3* (2), 22002.
- (5) Mlack, J. T.; Masih Das, P.; Danda, G.; Chou, Y.-C.; Naylor, C. H.; Lin, Z.; López, N. P.; Zhang, T.; Terrones, M.; Johnson, A. T. C.; Drndić, M. *Sci. Rep.* **2017**, *7* (1), 43037.
- (6) Parkin, W. M.; Balan, A.; Liang, L.; Das, P. M.; Lamparski, M.; Naylor, C. H.; Rodríguez-Manzo, J. A.; Johnson, A. T. C.; Meunier, V.; Drndić, M. *ACS Nano* **2016**, *10* (4), 4134–4142.
- (7) Feng, J.; Liu, K.; Graf, M.; Dumcenco, D.; Kis, A.; Di Ventra, M.; Radenovic, A. *Nat. Mater.* **2016**, *15* (8), 850–855.
- (8) Feng, J.; Graf, M.; Liu, K.; Ovchinnikov, D.; Dumcenco, D.; Heiranian, M.; Nandigana, V.; Aluru, N. R.; Kis, A.; Radenovic, A. *Nature* **2016**, *536*, 197–200.
- (9) Surwade, S. P.; Smirnov, S. N.; Vlassioux, I. V.; Unocic, R. R.; Veith, G. M.; Dai, S.; Mahurin, S. M. *Nat. Nanotechnol.* **2015**, *10* (5), 459–464.
- (10) Wang, L.; Boutilier, M. S. H.; Kidambi, P. R.; Jang, D.; Hadjiconstantinou, N. G.; Karnik, R. *Nat. Nanotechnol.* **2017**, *12* (6), 509–522.
- (11) Cohen-Tanugi, D.; Grossman, J. C. *Nano Lett.* **2012**, *12* (7), 3602–3608.
- (12) Cohen-Tanugi, D.; McGovern, R. K.; Dave, S. H.; Lienhard, J. H.; Grossman, J. C. *Energy Environ. Sci.* **2014**, *7* (3), 1134.
- (13) O'Hern, S. C.; Jang, D.; Bose, S.; Idrobo, J. C.; Song, Y.; Laoui, T.; Kong, J.; Karnik, R. *Nano Lett.* **2015**, *15* (5), 3254–3260.
- (14) O'Hern, S. C.; Stewart, C. A.; Boutilier, M. S. H.; Idrobo, J. C.; Bhaviripudi, S.; Das, S. K.; Kong, J.; Laoui, T.; Atieh, M.; Karnik, R. *ACS Nano* **2012**, *6* (11), 10130–10138.
- (15) Heiranian, M.; Farimani, A. B.; Aluru, N. R. *Nat. Commun.* **2015**, *6*, 8616.
- (16) Li, S.; Wang, S.; Tang, D. M.; Zhao, W.; Xu, H.; Chu, L.; Bando, Y.; Golberg, D.; Eda, G. *Appl. Mater. Today* **2015**, *1* (1), 60–66.
- (17) Splendiani, A.; Sun, L.; Zhang, Y.; Li, T.; Kim, J.; Chim, C. Y.; Galli, G.; Wang, F. *Nano Lett.* **2010**, *10* (4), 1271–1275.
- (18) Huang, P. Y.; Ruiz-Vargas, C. S.; van der Zande, A. M.; Whitney, W. S.; Levendorf, M. P.; Kevek, J. W.; Garg, S.; Alden, J. S.; Hustedt, C. J.; Zhu, Y.; Park, J.; McEuen, P. L.; Muller, D. A. *Nature* **2011**, *469* (7330), 389–392.
- (19) Dang, K. Q.; Spearot, D. E. *J. Appl. Phys.* **2014**, *116* (1), 01350810.1063/1.4886183
- (20) Lin, Y.-C.; Zhang, W.; Huang, J.-K.; Liu, K.-K.; Lee, Y.-H.; Liang, C.-T.; Chu, C.-W.; Li, L.-J. *Nanoscale* **2012**, *4* (20), 6637.
- (21) Mignuzzi, S.; Pollard, A. J.; Bonini, N.; Brennan, B.; Gilmore, I. S.; Pimenta, M. A.; Richards, D.; Roy, D. *Phys. Rev. B: Condens. Matter Mater. Phys.* **2015**, *91* (19), 1–7.
- (22) Carvalho, B. R.; Wang, Y.; Mignuzzi, S.; Roy, D.; Terrones, M.; Fantini, C.; Crespi, V. H.; Malard, L. M.; Pimenta, M. A. *Nat. Commun.* **2017**, *8*, 14670.
- (23) Tongay, S.; Suh, J.; Ataca, C.; Fan, W.; Luce, A.; Kang, J. S.; Liu, J.; Ko, C.; Raghunathanan, R.; Zhou, J.; Ogletree, F.; Li, J.; Grossman, J. C.; Wu, J. *Sci. Rep.* **2013**, *3* (1), 2657.

- (24) Mak, K. F.; He, K.; Lee, C.; Lee, G. H.; Hone, J.; Heinz, T. F.; Shan, J. *Nat. Mater.* **2013**, *12* (3), 207–211.
- (25) Chow, P. K.; Jacobs-Gedrim, R. B.; Gao, J.; Lu, T. M.; Yu, B.; Terrones, H.; Koratkar, N. *ACS Nano* **2015**, *9* (2), 1520–1527.
- (26) Carozo, V.; Wang, Y.; Fujisawa, K.; Carvalho, B. R.; McCreary, A.; Feng, S.; Lin, Z.; Zhou, C.; Perea-López, N.; Elías, A. L.; Kabius, B.; Crespi, V. H.; Terrones, M. *Sci. Adv.* **2017**, *3* (4), e1602813.
- (27) Ghorbani-Asl, M.; Kretschmer, S.; Spearot, D.; Krasheninnikov, A. V. *2D Mater.* **2017**, *110* (1), 76–91.
- (28) Lehtinen, O.; Kotakoski, J.; Krasheninnikov, A. V.; Tolvanen, A.; Nordlund, K.; Keinonen, J. *Phys. Rev. B: Condens. Matter Mater. Phys.* **2010**, *81* (15), 1–4.
- (29) Yoon, K.; Rahnamoun, A.; Swett, J. L.; Iberi, V.; Cullen, D. A.; Vlasiouk, I. V.; Belianinov, A.; Jesse, S.; Sang, X.; Ovchinnikova, O. S.; Rondinone, A. J.; Unocic, R. R.; Van Duin, A. C. T. *ACS Nano* **2016**, *10* (9), 8376–8384.
- (30) Komsa, H. P.; Kurasch, S.; Lehtinen, O.; Kaiser, U.; Krasheninnikov, A. V. *Phys. Rev. B: Condens. Matter Mater. Phys.* **2013**, *88* (3), 1–8.
- (31) Merchant, C. A.; Healy, K.; Wanunu, M.; Ray, V.; Peterman, N.; Bartel, J.; Fischbein, M. D.; Venta, K.; Luo, Z.; Johnson, A. T. C.; Drndić, M. *Nano Lett.* **2010**, *10* (8), 2915–2921.
- (32) Danda, G.; Masih Das, P.; Chou, Y.-C.; Mlack, J. T.; Parkin, W. M.; Naylor, C. H.; Fujisawa, K.; Zhang, T.; Fulton, L. B.; Terrones, M.; Johnson, A. T. C.; Drndić, M. *ACS Nano* **2017**, *11* (2), 1937–1945.
- (33) Zhou, Z.; Hu, Y.; Wang, H.; Xu, Z.; Wang, W.; Bai, X.; Shan, X.; Lu, X. *Sci. Rep.* **2013**, *3*, 3287.
- (34) Liu, K.; Feng, J.; Kis, A.; Radenovic, A. *ACS Nano* **2014**, *8* (3), 2504–2511.
- (35) Feng, J.; Liu, K.; Graf, M.; Lihter, M.; Bulushev, R. D.; Dumcenco, D.; Alexander, D. T. L.; Krasnozhan, D.; Vuletic, T.; Kis, A.; Radenovic, A. *Nano Lett.* **2015**, *15* (5), 3431–3438.
- (36) Venta, K.; Shemer, G.; Puster, M.; Rodríguez-Manzo, J. A.; Balan, A.; Rosenstein, J. K.; Shepard, K.; Drndić, M. *ACS Nano* **2013**, *7* (5), 4629–4636.
- (37) Rodríguez-Manzo, J. A.; Puster, M.; Nicolai, A.; Meunier, V.; Drndić, M. *ACS Nano* **2015**, *9* (6), 6555–6564.
- (38) Shekar, S.; Niedzwiecki, D. J.; Chien, C. C.; Ong, P.; Fleischer, D. A.; Lin, J.; Rosenstein, J. K.; Drndić, M.; Shepard, K. L. *Nano Lett.* **2016**, *16* (7), 4483–4489.
- (39) Marcus, Y. *J. Solution Chem.*, **1983**, *12* (3).27110.1007/BF00646201
- (40) Feng, J.; Liu, K.; Graf, M.; Dumcenco, D.; Kis, A.; Di Ventura, M.; Radenovic, A. *Nat. Mater.* **2016**, *15* (8) (Suppl. 1), 850–855.10.1038/nmat4607
- (41) Koch, C. Determination of Core Structure Periodicity and Point Defect. PhD. Thesis, Arizona State University, May 2002.
- (42) Perez, B.; Senet, P.; Meunier, V.; Nicolli, A. *WSEAS Trans. Circuits Syst.* **2017**, *16*, 35–44.
- (43) Wei, G.; Quan, X.; Chen, S.; Yu, H. *Phys. Rev. A* **2017**, *11* (2), 1960–1926.
- (44) Hille, B. J. *Gen. Physiol.* **1968**, *51* (2), 199–219.

■ NOTE ADDED AFTER ASAP PUBLICATION

This paper published ASAP on 3/1/2108. Figure 1, panel e, was corrected and the revised version was reposted on 3/14/2018.